Atomic force microscopy imaging and nanomechanical properties of six Tau isoforms assemblies

Ali Makky, Luc Bousset, Karine Madiona, Ronald Melki

Journal Pre-proof

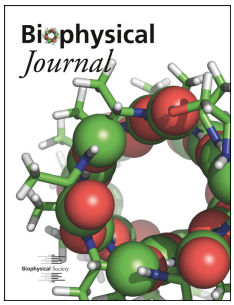

Atomic force microscopy imaging and nanomechanical properties of six Tau isoforms assemblies

Ali Makky, Luc Bousset, Karine Madiona, Ronald Melki

PII: S0006-3495(20)30893-6

DOI: https://doi.org/10.1016/j.bpj.2020.10.045

Reference: BPJ 10674

To appear in: *Biophysical Journal*

Received Date: 15 June 2020

Accepted Date: 9 October 2020

Please cite this article as: Makky A, Bousset L, Madiona K, Melki R, Atomic force microscopy imaging and nanomechanical properties of six Tau isoforms assemblies, *Biophysical Journal* (2020), doi: https://doi.org/10.1016/j.bpj.2020.10.045.

Atomic force microscopy imaging and nanomechanical properties of six Tau isoforms assemblies

Ali Makky*[1], Luc Bousset[2], Karine Madiona[2], Ronald Melki*[2]

[1] Institut Galien Paris-Sud, CNRS, Université Paris-Sud, Université Paris-Saclay, Châtenay-Malabry, France

[2] Institut Fancois Jacob (MIRCen), CEA and Laboratory of Neurodegenerative Diseases, CNRS, Fontenay-Aux-Roses, France

Correspondence to Ali Makky, ali.makky@universite-paris-saclay.fr or Ronald Melki, ronald.melki@cnrs.fr

KEYWORDS

Tauopathies, tau protein isoforms, Atomic force microscopy, fibrils, polymorphs

STATEMENT OF SIGNIFICANCE

The aggregation of the protein tau is intimately associated with tauopathies such as Alzheimer's disease. This study shows that the six different Tau isoforms form fibrils consisting of two protofibrils separated by a shallow groove. We show that Tau N-terminal inserts do not contribute to any morphological or mechanical difference among isoforms. Fibrils made of Tau molecules with four carboxyl□terminal microtubule binding domains have a persistence length two-fold higher than those with three domains. The axial and radial Young's moduli we determined are significantly lower than those of other amyloids suggesting weak intermolecular

interaction between the paired β-sheets within Tau fibrils. The results show that Tau fibrils are labile, a property essential for their prion-like propagation propensity.

ABSTRACT

The amyloid fibrillar form of the protein Tau is involved in a number of neurodegenerative diseases, also known as tauopathies. In this work, six different fibrillar Tau isoforms were assembled in vitro. The morphological and nanomechanical properties of these isoforms were studied using atomic force microscopy at high resolution in air and buffer. Our results demonstrate that all Tau isoforms fibrils exhibit paired helical filaments (PHF)-like structures consisting of two protofibrils separated by a shallow groove. Interestingly, whereas the N-terminal inserts do not contribute to any morphological or mechanical difference between the isoforms with the same carboxyl□terminal microtubule binding domain repeats, isoforms with 4 microtubules repeats (4R) exhibited a persistence length ranging from 2.0 to 2.8 µm, almost two fold higher than those with 3 repeats (3R). In addition, the axial Young's modulus values derived from the persistence lengths as well as their radial ones determined via nanoindentation experiments, were very low compared to amyloid fibrils made of other proteins. This sheds light on the weak intermolecular interaction acting between the paired β-sheets within Tau fibrils. This may play an important role in their association into high molecular weight assemblies, into their dynamics, their persistence, their clearance in cells and their propagation.

INTRODUCTION

Six isoforms of the microtubule associated protein Tau are produced from the alternative splicing of the pre-mRNA encoded by the 16 exons of the *MAPT* gene. Those isoforms differ from each

other by the absence or the presence of 1 or 2 N-terminal inserts that modulate Tau interaction with cell membranes and tyrosine kinase. The protein is then termed 0, 1 or 2 N Tau. They also differ by the number of repeated amino-acid stretches located within the C-terminal domain of the protein through which they bind to microtubules. When Tau exon 10, that encodes the second of four microtubule-binding domains, is lacking, Tau isoform comprises 3 instead of 4 microtubule-binding domains. The proteins are termed 3R and 4R, respectively (1).

The aggregation of Tau into high molecular weight assemblies that exhibit characteristics phosphorylation patterns is intimately linked to several tauopathies, ranging from Alzheimer's disease (AD) to Pick's disease (PiD), Tangle only dementia, Progressive Supranuclear Palsy, Frontotemporal dementia, Corticobasal neurodegeneration (CBD), Argyrophilic grain disease or Chronic traumatic encephalopathy (CTE)(2). All Tau isoforms assemble into high molecular weight particles that have fibrillar shape when extracted in the presence of detergents from the brains of patients. The latter fibrils are believed to possess prion-like properties. They spread and seed the aggregation of endogenous Tau, thus leading to increased pathology (3). The aggregation of recombinant Tau into long unbranched fibrils can be achieved in vitro in the presence of the glycosaminoglycan heparin (4). The structure of the protease resistant amyloid core of fibrillar Tau purified in the presence of detergents from the brains of patients who developed AD, PiD, CBD and CTE has been recently solved by cryo-electron microscopy (5-7). The core of AD and CTE patients-derived fibrils is built from the microtubule-binding repeats R3 and R4 and ten additional amino acids from the C-terminal flanking region. It spans residues 273/304-380 (2N4R Tau numbering). The core structure of CBD spans residues K274-E380 e.g. the last residue of R1, the repeats R2, R3 and R4, as well as the 12 following C-terminal amino acid residues (8-9). For PiD-derived Tau filaments, the core is longer. It spans residues 254-378,

includes the 20 C-terminal amino-acids of R1, in addition to the R3 and R4 repeats and the ten residues following the R4 repeat (5, 10). Furthermore, while fibrils purified from AD are made of two protofilaments, arranged in two different manners, those purified from PiD and CBD brains are made sometimes of a single protofilament, sometimes of two. The structure of fibrillar Tau generated in the presence of heparin has also been assessed by cryo-electron microscopy (7). Besides spanning fewer (47-58) amino acid residues, the pronase-resistant core of fibrils made de novo from Tau 2N3R and 2N4R isoforms appears to adopt different folds, distinct from that of patient-derived fibrillar particles, and to be made of a single protofilament for 4R Tau as opposed to two protofilaments for 3R Tau.

Here we assessed the physical properties of fibrils assembled from the 6 different Tau isoforms by atomic force microscopy in air and buffer. We show that all fibrils exhibit PHF-like structures consisting of two protofibrils aligned together and separated by a shallow groove. We show that the N-terminal inserts, most probably constituting the fibrils "fuzzy coat", do not contribute to fibril height and width. A statistical analysis of the shape and thermal shape fluctuations (11-13) is presented. Tau isoforms with 4 microtubules repeats exhibited a persistence length ranging from 2.0 to 2.8 µm, almost two fold higher than those with 3 repeats (~ 1 µm). Overall, Tau fibrils exhibit very low axial and radial Young's moduli compared to other amyloid fibrils.

MATERIALS AND METHODS

Tau isoforms purification and assembly

Recombinant wild-type, full-length human Tau isoforms were expressed and purified as described previously (14). Tau protein concentration was determined by spectrophotometry using an extinction coefficient of 7,450 per M/cm at 280 nm. Aliquots of pure Tau proteins at

concentrations of 50–100 μM in PBS buffer supplemented with 1mM ß-mercaptoethanol were stored at −80°C. Fibrillation of Tau was achieved at 40 μM in PBS in the presence of 10 μM heparin by shaking 0.5 ml solution aliquots at 37°C in an Eppendorf Thermomixer set at 600 rpm for 4 days. Assembly completion was assessed by Thioflavin T fluorescence measurement.

Transmission electron microscopy (TEM)

The shape of fibrillar Tau isoforms was assessed using a JEOL 1400 transmission electron microscope following adsorption onto carbon-coated 200-mesh grids and negative staining with 1% uranyl acetate. The images were recorded with a Gatan Orius CCD camera (Gatan).

Atomic force microscopy imaging

The different fibrillar Tau assemblies (20 μM) were first diluted in milli-Q water to a final concentration of ~ 10 μg/ml. Afterwards, 100 μl of the diluted fibrils solutions were deposited on either freshly cleaved mica (muscovite mica, grade V1 from Ted Pella Inc.) substrates and left overnight to allow the evaporation of water at a constant temperature (25 °C).

The AFM imaging of Tau fibrils was performed in ambient conditions at room temperature (25 °C) using a JPK Nanowizard Ultraspeed AFM from JPK instruments in amplitude modulation AFM (AM-AFM) with low force settings (80–90% of the free amplitude A ~10 nm). Gold coated silicon ACTG cantilevers (nominal spring constant ~37 nN/nm, tip radius < 10 nm) from AppNano (USA) have been used.

For each sample, a large number of fibrillar assemblies were systematically imaged at high resolution (3 μm x 3μm or 5μm × 5 μm at 1024 × 1024 pixels) with AFM and their morphology

(height and width) were analyzed manually with the JPK Data Processing software (JPK Instruments) using the line profile measurement option.

The width of Tau fibrils was determined manually from images recorded in phase modulation AFM (PM-AFM) (15-16) using ultrasharp AFM tips cantilevers Hi'Res-C15/Cr-Au-5 with a tip radius of ~1 nm (Mikromasch) and a spring constant of ~42 N/m (15). The image size in this case was not higher than 1 μm × 1 μm to preserve the tip sharpness and only few numbers of images at high resolution (1 μm × 1 μm, 512 x 512 or 1024 × 1024 pixels) have been performed with the same tip to minimize tip convolution effect. In PM-AFM, the constant amplitude was kept at ~15 nm and the phase setpoint was 1°. Images were recorded at a scan rate of 0.5-1 Hz. Despite the use of ultrasharp tips, the determined width values were higher than those derived from transmission electron micrographs (TEM). Thus, we have adopted the latter for the calculation of the second moment of areas as shown in figure S1, table S1 and explained in the supporting methods. In addition, it should be noted that fibrils exhibited higher heights (table S2) as determined from AFM images obtained with JPK Quantitative imaging mode (QI) in PBS which could be due to the swelling of the fuzzy coat. As Tau fibrils hydration did not impact significantly their persistence length and in order to avoid any potential underestimation of the axial Young's modulus, we have used the measured height from AFM images in air and the measured width from TEM images for the calculation of the second moment of area as explained in the next section.

Persistence length, bending rigidity and axial Young's modulus calculation

The persistence length (P_l) of Tau fibrils imaged in air, was analyzed using the open source software "Easyworm" developed by Lamour et al.(12) as described in our previous work(15).

Only intact and isolated fibrils of at least 600 nm in length were included in the analysis. The contour lengths distributions of the analyzed fibrils are shown in Figure S2.

The calculation of the P_l can be done using three different expressions (the bond correlation functions $<\cos\theta>$, mean square of the deviations $<\delta^2>_{2D}$ to secant midpoints as a function of the distance) and the mean-squared end-to-end distance $<R^2>_{2D}$ all derived from Worm-like chain (WLC) model for semi-flexible polymers (11-12, 15, 17). However, as most of the analyzed contour lengths of fibrils were lower than their persistence lengths as shown in Figure S2, only those obtained with secant midpoints method were used for the determination of the bending rigidity (κ) and the axial Young's modulus (12-13). All the details about these calculations can be found in the supporting methods.

From the persistence length, the bending rigidity (κ) was calculated using the following equation:

$$\kappa = K_B.T.P_l \qquad (1)$$

Where T is the room temperature (298 °K) and K_B is the Boltzmann constant.

The axial Young's modulus (E) was then calculated from the bending rigidity using the following equation:

$$E = \frac{\kappa}{I} \qquad (2)$$

Where I is the second moment of area (or moment of inertia), which was calculated using the tape-like model because Tau fibrils exhibited lower heights compared to their widths. As the bending energy is proportional to the thermal energy (K_B.T) needed to bend the fibrils, it reflects the lowest energy bending mode that corresponds to the one obtained with the lowest moment of inertia. The latter was calculated using the tape-like model depending on the geometry of the

cross-sectional area of the imaged fibrils (12-13, 15, 18) as explained in the supporting methods and table S3.

Impact of water evaporation on the persistence lengths of Tau fibrils

To assess the impact of water evaporation on the persistence lengths of Tau assemblies, we performed AFM imaging in buffer conditions. To do so, 100 µL of fibrillar Tau assemblies at a concentration of 30 µg/mL in milli-Q water were deposited onto mica substrate and incubated for 60 minutes at room temperature. The excess of Tau fibrils was then gently removed by exchanging the sample solution against PBS buffer. Afterwards, AFM imaging was carried out using Gold coated nitride Lever (SNL-A) probes (Bruker, Santa Barbara, CA) with a nominal spring constant of ~0.35 N/m and a tip radius of 2 nm, in a homemade fluid cell containing 200 µL of PBS buffer, at room temperature in JPK Quantitative imaging™ (QI) mode (19-20) with a resolution of 3.5 µm × 3.5 µm, 512 × 512 pixels. The force setpoint was fixed to 550-800 pN at an indentation speed of 15 µm/s. In order to avoid the tip damage, the cantilever sensitivity was determined at the end of the AFM experiments by performing force curve spectroscopy on mica substrate in PBS buffer. The spring constant of the cantilever was then measured in PBS buffer at room temperature and determined using the equipartition theorem (thermal noise) (21-22) implemented in the JPK software Calibration Manager. QI™ is a multiparametric mode that collects force-distance (FD) curves in each pixel of a high-resolution image with information about height, sample stiffness and adhesion. At each scanned pixel, the cantilever approached the surface until the vertical deflection reached the setpoint value, inducing sample's deformation, before being retracted away (20). This movement algorithm thus prevents the lateral forces which are problematic for loosely attached samples. As shown in figure S4, the AFM images obtained in PBS or in air demonstrate that Tau fibrils exhibit similar shapes and orientation (Figures 1, 2,

4). Moreover, 1N3R and 1N4R Tau fibrils in PBS displayed persistence length values similar to those obtained in ambient air. This implies that the preparation conditions we used, allowed the fibrils to equilibrate on mica surface when imaged in ambient air.

Radial Young's modulus determination from nanoindentation experiments

To assess the reliability of the axial Young's modulus values calculated from the persistence lengths, we studied the radial modulus of Tau fibrils using JPK Quantitative imaging™ (QI) mode with a resolution of 3.5 µm × 3.5 µm (or 5 x 5 µm) , 512 × 512 pixels, as described above.

The Young's modulus associated with each pixel was determined with the JPK Data Processing software using the Hertz model. To do so, the approaching part of the force-indentation curves was fitted using the force-indentation relationship described in the Hertz model for the spherical indenter, as described by the following equation (3)

$$F = \frac{4}{3}.\frac{E}{1-\nu^2}.\sqrt{r}.\delta^{\frac{3}{2}} \qquad (3)$$

where ν is the Poisson's ratio set at 0.5 (a typical value retained for incompressible isotropic materials), δ the sample deformation induced by the indentation, r the tip radius estimated at 2 nm, F the force applied during sample indentation and E the elastic modulus also called apparent Young's modulus. This allowed the generation of the corresponding elasticity map. In these experiments, the force setpoint was fixed to 0.7-0.8 nN at an indentation speed of 16.7 µm/s.

As the Hertz model is valid for small indentations going up to 20 % of the material's height, and given that fibril height is ~10 nm, the approach force curves were fitted up to a force setpoint of 0.2 nN which maintains a sample deformation of approximately 2 nm. At such small

deformations, the result is not biased by the underlying substrate's rigidity and the contact area between the tip and the indented material does not exceed the tip radius (Figure S5).

RESULTS AND DISCUSSION

Analysis of the morphology of Tau fibrils isoforms

In this work we assessed the morphological properties by TEM and AFM in ambient air of six Tau fibrils isoforms that were assembled *in vitro*. Tau isoforms (Figure 1) are named 0N3R, 0N4R, 1N3R, 1N4R, 2N3R and 2N4R, based on the number of amino□terminal exon inserts (0N, 1N, and 2N) or carboxyl□terminal microtubule binding domain repeats (3R and 4R). These isoforms are normally expressed in the central nervous system. Whereas 0N Tau are seen solely in the fetal brain, the other isoforms are found in the adult brain (23). First, we used ultrasharp AFM probes in order to assess the structural morphology of tau isoforms in ambient air in PM-AFM imaging mode. Indeed, several studies have pointed out that Tau proteins can assemble into fibrillar aggregates commonly referred to as paired helical filaments (PHFs) (24-26), others reported that they consisted in ribbon-like structures (27).

As shown in Figures 1 and 2, all Tau isoforms fibrillar assemblies exhibited PHFs structure which consists of two protofibrils aligned together and separated by a shallow groove throughout the length of Tau fibril. In some cases, the separating grooves between the two protofibrils were not seen (Figure 1b-f, green arrows) and Tau fibrils appeared thinner with higher height than those exhibiting separating grooves. This could be due to the orientation of adsorbed particles onto mica. Indeed, whereas most fibrils lie flat on their largest surface, others may lie on their edge. Moreover, while some fibrils did not show any twist, others exhibited some twists along their length as depicted in the TEM images (Figure 3). Furthermore, and independently of the

Tau isoform, fibrils adopted straight, curved or wavy conformation when adsorbed on either mica or the carbon film of the electron microscopy grid.

Next, we analyzed the morphological characteristics of the fibrils assembled from the six isoforms and results are presented in table 1. Tau fibrils imaged by AFM in air, revealed widths between 18-20 nm and heights comprised between 5 and 7 nm. TEM images revealed lower widths in the order of ~12-13 nm for all tau fibrils (Figure S1, table S1). This may be due to tip convolution effect despite the use of ultrasharp tips. Hence only widths measured by TEM were used in the calculation of the second moment of area of Tau fibrils.

The measured height values in air are very low compared to those determined by other authors who reported Tau fibrils thickness ranging from 11 to 18.5 nm (27-28) for the same sample of Tau 2N4R depending on the AFM imaging conditions (i.e. in air or liquid, ionic strength) and imaging mode. Furthermore, it should be noted that the same authors (27) observed within the same sample two different fibril shapes, that were classified either into thin or thick fibrils. Thin and thick Tau 2N4R fibrils exhibited heights ranges 9.8-14.5 nm and 11.5-18.5 nm, respectively. Such difference could be related to fibrils polymorphism that mainly depends on the preparation method of fibrils. We did not observe thin and thick fibrils (27-28) in our fibrillar preparations. The fibrils were highly homogenous instead. This may explain the lower measured height values presented here. Besides, the height reduction of Tau fibrils imaged in air may be caused by fibrils drying artifacts and/or by the AFM imaging mode and conditions (13, 29-30). Thus, in order to evaluate the impact of drying on fibril height, we have imaged the same fibrils in PBS buffer using QI imaging mode by applying low imaging forces (~ 550-600 pN). Our results demonstrated a significant increase in Tau fibril height when imaged in buffer (Table S2). Depending on the Tau isoform, the height ranged from 8 to 11 nm (Table S2). Interestingly, 4R tau isoforms exhibited a higher thickness (height) than their 3R counterparts independently from

the number of amino□terminal inserts (0N, 1N or 2N). This suggests that the carboxyl□terminal microtubule binding domain repeats (3R or 4R), but not the N-terminal inserts, contribute significantly to fibril height. This is in agreement with the widely accepted view that Tau N-terminal domain is unstructured and flexible, constituting the "fuzzy coat" surrounding Tau fibril amyloid core (28). Such disordered domains, cannot be directly measured by conventional AFM imaging techniques (i.e. AM-AFM or contact modes) (27). In fact, Wegmann et al. (28) could measure the height differences between fibrils of recombinant full-length 2N4R and fibril amyloid core lacking most of the terminal Tau domains only by analyzing their deformation maps either in different ionic strength conditions or different force setpoints using PeakForce Tapping mode (28).

Nanomechanical properties of the different Tau fibrillar isoforms

As the AFM analysis of the different Tau isoforms either in air or buffer did not reveal significant differences in fibrils shapes and morphological characteristics (Figure S4), we decided to measure their persistence lengths (P_l) and their cross-sectional second moment of area (I). This allows determining their Bending rigidity (κ) and their axial Young's modulus (K) respectively, thus providing a better understanding of their nanomechanical properties (12-13, 15, 18). Indeed, fibril rigidity influences the frequency with which they break, which in turn has an impact on the kinetics of fibrils growth. To this aim, we performed a statistical analysis of the shape thermal fluctuations of the different Tau fibrillar isoforms adsorbed onto mica substrate and imaged with AFM in ambient air. The contour length of isolated fibrillar assemblies from topographical images were tracked semi-automatically using Easyworm software and the persistence length(12) (P_l) was calculated using the mean square of the deviations $<\delta^2>_{2D}$ to secant midpoints approach derived from the WLC model for semi-flexible polymers as reported previously (12-13).

Figures 4 and 5 show AFM height images (4a-4c, 5a-5c) of the six Tau isoforms fibrillar assemblies in air, their contour lengths (4d-4f, 5d-5f) and the mean square of the deviations <δ2> 2D to secant midpoints plots as the function of the length (4g-4i, 5g-5i). The calculated P_l values are listed in Table 1. The P_l values demonstrated that the distinct fibrillar assemblies exhibit different mechanical properties depending on the carboxyl□terminal microtubule binding domain repeats (either 3R or 4R) of Tau isoforms. Indeed, Tau isoforms with 4 domains repeats exhibited a P_l ranging from 1.9 to 2.8 µm, in agreement with those measured by Wegmann et al(27), which are almost two fold higher than those with 3 repeats (1.1 – 1.2 µm) independently of the amino□terminal inserts (0N, 1N or 2N). In addition, the bending rigidity followed the same trend suggesting that 4R Tau fibrils were more rigid than 3R Tau fibrils.

Next, we aimed to determine Tau fibrils axial Young's modulus. Thus, we calculated the second moment of area (I) from the average heights measured in air and widths of fibrils measured by TEM. As shown in table 1, the cross-sectional assessment (average height of ~6 nm and width of ~12 nm) of the imaged fibrils fits with "ribbon-like" particles with rectangular cross section. The results presented in Table 1, revealed that Tau fibrils exhibit very low axial Young's modulus compared to other amyloid fibrils showing values ranging from 2 to 14 GPa (17-18, 31-34). Such difference could not be only related to potential errors in the cross sectional measurements of the fibrils which may lead to an underestimation of the calculated axial Young's modulus but rather to different intrinsic structures between the different amyloids and to the intermolecular interactions (18) between Tau monomers that stabilize fibrils structure (18, 35). Indeed, by measuring the persistence lengths of eight different types of amyloids fibrils, Knowles et al.(18) highlighted the relative importance of backbone hydrogen bonding in modulating fibrils rigidities. In addition, distinct fibrils were sorted into different classes of biomaterials upon

plotting their bending rigidities as a function of their moment of inertia (13, 18). It should be noted that the stiffness can vary significantly between amyloid fibrils depending on the density of intermolecular hydrogen bonding (18, 36). Importantly, Nassar et al(36) have recently studied the relation between the nanomechanical properties of amyloid fibrils, the intermolecular H-Bonds density and their size. By plotting the axial Young's moduli as a function of the rectangular cross-sectional area of seventeen different amyloids, the authors found that the axial Young's modulus is inversely correlated with their cross-sectional area (36). With the aid of molecular dynamics simulations (MDs), authors also found that compared to amyloids with large cross sections, fibrils with narrow ones can optimize the packing densities of residues and intermolecular H-bonds and exhibited higher stiffness (36).

Following the same line of thoughts and since the studied Tau fibrils isoforms have large cross-sectional area compared to other amyloids described in the literature, the intermolecular H-bonds as well as the packing densities between the residues in Tau fibrils should be lower than other narrower amyloids thus providing lower Young's modulus. Thus, by implementing the measured rectangular cross sectional areas of Tau fibrils in the inverse correlation equation uncovered by Nassar et al. (36), we found that the calculated Young's modulus values were strongly consistent with the predicted ones (Figure 6A). This demonstrates the reliability of the determined Young's moduli calculated in this work.

Next, we represented in Figure 6B the bending rigidity values as a function of their moment of inertia (I) for ribbon-like particles. The plot reveals that Tau fibrils made of the six isoforms exhibit Young modulus values below 0.03 GPa and lie between the (i) region where the molecules are held together within a particle by amphiphilic interactions (region labeled in green) and (ii) the region, labeled yellow, that corresponds to entropic elasticity (Figure 6B).

The nanomechanical properties of Tau fibrils were further assessed by determining their radial Young's modulus using JPK Quantitative imaging™ (QI) mode (19-20). The spring constant of the imaged fibrils and their Young's modulus were determined by fitting the slope and the approach curves, respectively. As shown in Figures 7-8 and Table S5, the measured Young's moduli are within the same order of magnitude of those determined from the persistence length measurements and the spring constant values we measured are similar to those determined by other authors (28). It should be noted, that the slightly higher values obtained by nanoindentation experiments could be due either to the mechanical anisotropy due to the heterogeneity of the inner structure of amyloids fibrils (37) or to the finite sample thickness compared to the indentation depth, where the cantilever 'feels' not only the sample but also the underlying substrate with subsequent overestimation of the radial Young's modulus.

Taken together, our results thus suggest that Tau molecules are held together within the fibrillar assemblies by relatively weak intermolecular forces compared to intramolecular ones (35). Similar properties were described for less-organized protofibrillar structures such as α-lactalbumin (α-lac) and αB-crystallin (αB) (18) but also for mouse prion nanofibrils (PrP) (13) that exhibited high intrinsic flexibility. Such weak intermolecular forces may play an important role in Tau molecules association into high molecular weight assemblies, into the dissociation of those assemblies, in their persistence and clearance in cells and their propagation (18, 38-40). The weakness of the intermolecular forces within Tau fibrillar scaffold were further supported by the observation that the fibrils disassemble during AFM imaging in PBS at high loading forces (> 700 pN) as shown in Figure S6. Similar results were obtained by Wegmann et al. (28) who observed that increasing the applied force during AFM imaging led to the disassembly of 2N4R Tau fibrils into small fragments with the presence of thread-like connections between the

remaining fibrils. Such disassembly was also observed by changing the ionic strength or by adsorption of Tau fibrils to HOPG hydrophobic surfaces (28).

CONCLUSIONS

In this work, we generated Tau amyloid fibrils assembled in vitro from six Tau protein isoforms. The different Tau fibrils were then imaged at high resolution by AFM either in air or in buffer. We show that independently from the protein isoform, all fibrils exhibited paired helical filaments (PHFs) structure. Interestingly, whereas the N-terminal inserts that most probably constitute the fibrils "fuzzy coat", do not contribute to any morphological or mechanical difference between the isoforms with the same carboxyl□terminal microtubule binding domain repeats, isoforms with 4 microtubules repeats (4R) exhibited persistence lengths almost two fold higher than those with 3 repeats (3R). In addition, the derived axial Young's modulus values are very low compared to other amyloid fibrils, thus shedding light on the weak intermolecular interaction acting between the paired β-sheets of Tau proteins that would play an important role in their association/dissociation but also in their toxicity and propagation mechanisms. However, to validate this hypothesis and in order to correlate the determined nanomechanical properties with structural differences between the six isoforms, further structural and functional characterization are necessary.

SUPPORTING MATERIAL

Supplementary methods, six figures and five tables are available as supporting material.

AUTHOR CONTRIBUTIONS

A.M., L.B. and R.M. designed the study; L.B. and K.M. prepared the different fibrillar samples. L.B. performed TEM imaging; A.M. performed AFM imaging and analysis. A.M. and R.M. wrote the manuscript.

ACKNOWLEDGMENTS

The authors thank Tracy Bellande for expert technical assistance. This study was supported by the Centre National de la Recherche Scientifique and grants from the Fondation Pour La Recherche Médicale (contract DEQ. 20160334896 and ALZ201912009776) and the EU Joint Programme on Neurodegenerative Disease Research (JPND) and Agence National de la Recherche (contracts PROTEST-70, ANR-17-JPCD-0005-01 and TransPathND, ANR-17-JPCD-0002-02). This work benefited from the electron microscopy facility of Imagerie-Gif. The authors are indebted to the Reviewers for their constructive suggestions.

REFERENCES

1. Goedert, M., M. G. Spillantini, R. Jakes, D. Rutherford, and R. A. Crowther. 1989. Multiple isoforms of human microtubule-associated protein tau: sequences and localization in neurofibrillary tangles of Alzheimer's disease. Neuron 3(4):519-526.
2. Spillantini, M. G., and M. Goedert. 2013. Tau pathology and neurodegeneration. Lancet Neurol 12(6):609-622.
3. Brundin, P., R. Melki, and R. Kopito. 2010. Prion-like transmission of protein aggregates in neurodegenerative diseases. Nat Rev Mol Cell Biol 11(4):301-307.
4. Goedert, M., R. Jakes, M. G. Spillantini, M. Hasegawa, M. J. Smith, and R. A. Crowther. 1996. Assembly of microtubule-associated protein tau into Alzheimer-like filaments induced by sulphated glycosaminoglycans. Nature 383(6600):550-553.
5. Falcon, B., W. Zhang, A. G. Murzin, G. Murshudov, H. J. Garringer, R. Vidal, R. A. Crowther, B. Ghetti, S. H. W. Scheres, and M. Goedert. 2018. Structures of filaments from Pick's disease reveal a novel tau protein fold. Nature 561(7721):137-140.
6. Goedert, M., B. Falcon, W. Zhang, B. Ghetti, and S. H. W. Scheres. 2018. Distinct Conformers of Assembled Tau in Alzheimer's and Pick's Diseases. Cold Spring Harb Symp Quant Biol 83:163-171.
7. Zhang, W., B. Falcon, A. G. Murzin, J. Fan, R. A. Crowther, M. Goedert, and S. H. W. Scheres. 2019. Heparin-induced tau filaments are polymorphic and differ from those in Alzheimer's and Pick's diseases. Elife 8:e43584.
8. Zhang, W., A. Tarutani, K. L. Newell, A. G. Murzin, T. Matsubara, B. Falcon, R. Vidal, H. J. Garringer, Y. Shi, T. Ikeuchi, S. Murayama, B. Ghetti, M. Hasegawa, M. Goedert, and S. H. W. Scheres. 2020. Novel tau filament fold in corticobasal degeneration. Nature 580(7802):283-287.

9. Arakhamia, T., C. E. Lee, Y. Carlomagno, D. M. Duong, S. R. Kundinger, K. Wang, D. Williams, M. DeTure, D. W. Dickson, C. N. Cook, N. T. Seyfried, L. Petrucelli, and A. W. P. Fitzpatrick. 2020. Posttranslational Modifications Mediate the Structural Diversity of Tauopathy Strains. Cell 180(4):633-644 e612.
10. Fitzpatrick, A. W. P., B. Falcon, S. He, A. G. Murzin, G. Murshudov, H. J. Garringer, R. A. Crowther, B. Ghetti, M. Goedert, and S. H. W. Scheres. 2017. Cryo-EM structures of tau filaments from Alzheimer's disease. Nature 547(7662):185-190.
11. Usov, I., and R. Mezzenga. 2015. FiberApp: An Open-Source Software for Tracking and Analyzing Polymers, Filaments, Biomacromolecules, and Fibrous Objects. Macromolecules 48(5):1269-1280.
12. Lamour, G., J. B. Kirkegaard, H. Li, T. P. Knowles, and J. Gsponer. 2014. Easyworm: an open-source software tool to determine the mechanical properties of worm-like chains. Source Code Biol Med 9:16.
13. Lamour, G., C. K. Yip, H. Li, and J. Gsponer. 2014. High intrinsic mechanical flexibility of mouse prion nanofibrils revealed by measurements of axial and radial Young's moduli. ACS Nano 8(4):3851-3861.
14. Tardivel, M., S. Begard, L. Bousset, S. Dujardin, A. Coens, R. Melki, L. Buee, and M. Colin. 2016. Tunneling nanotube (TNT)-mediated neuron-to neuron transfer of pathological Tau protein assemblies. Acta Neuropathol Commun 4(1):117.
15. Makky, A., L. Bousset, J. Polesel-Maris, and R. Melki. 2016. Nanomechanical properties of distinct fibrillar polymorphs of the protein alpha-synuclein. Sci Rep 6:37970.
16. Makky, A., T. Berthelot, C. F. Tarisse, H. Volland, P. Viel, and J. Polesel-Maris. 2012. Substructures high resolution imaging of individual IgG and IgM antibodies with piezoelectric tuning fork atomic force microscopy. Sensor Actuat B-Chem 162(1):269-277.
17. Adamcik, J., C. Lara, I. Usov, J. S. Jeong, F. S. Ruggeri, G. Dietler, H. A. Lashuel, I. W. Hamley, and R. Mezzenga. 2012. Measurement of intrinsic properties of amyloid fibrils by the peak force QNM method. Nanoscale 4(15):4426-4429.
18. Knowles, T. P., A. W. Fitzpatrick, S. Meehan, H. R. Mott, M. Vendruscolo, C. M. Dobson, and M. E. Welland. 2007. Role of intermolecular forces in defining material properties of protein nanofibrils. Science 318(5858):1900-1903.
19. Smolyakov, G., C. Formosa-Dague, C. Severac, R. E. Duval, and E. Dague. 2016. High speed indentation measures by FV, QI and QNM introduce a new understanding of bionanomechanical experiments. Micron 85:8-14.
20. Chopinet, L., C. Formosa, M. P. Rols, R. E. Duval, and E. Dague. 2013. Imaging living cells surface and quantifying its properties at high resolution using AFM in QI™ mode. Micron 48:26-33.
21. Hutter, J. L., and J. Bechhoefer. 1993. Calibration of atomic-force microscope tips. Review of Scientific Instruments 64:1868-1873.
22. Lévy, R., and M. Maaloum. 2001. Measuring the spring constant of atomic force microscope cantilevers: thermal fluctuations and other methods. Nanotechnology 13(1):33-37.
23. Goedert, M., M. G. Spillantini, M. C. Potier, J. Ulrich, and R. A. Crowther. 1989. Cloning and sequencing of the cDNA encoding an isoform of microtubule-associated protein tau containing four tandem repeats: differential expression of tau protein mRNAs in human brain. The EMBO Journal 8(2):393-399.
24. Kidd, M. 1963. Paired Helical Filaments in Electron Microscopy of Alzheimer's Disease. Nature 197(4863):192-193.
25. von Bergen, M., S. Barghorn, S. A. Müller, M. Pickhardt, J. Biernat, E.-M. Mandelkow, P. Davies, U. Aebi, and E. Mandelkow. 2006. The Core of Tau-Paired Helical Filaments Studied by Scanning Transmission Electron Microscopy and Limited Proteolysis. Biochemistry 45(20):6446-6457..

26. Barghorn, S., P. Davies, and E. Mandelkow. 2004. Tau Paired Helical Filaments from Alzheimer's Disease Brain and Assembled in Vitro Are Based on β-Structure in the Core Domain. Biochemistry 43(6):1694-1703.
27. Wegmann, S., Y. J. Jung, S. Chinnathambi, E.-M. Mandelkow, E. Mandelkow, and D. J. Muller. 2010. Human Tau Isoforms Assemble into Ribbon-like Fibrils That Display Polymorphic Structure and Stability. Journal of Biological Chemistry 285(35):27302-27313.
28. Wegmann, S., I. D. Medalsy, E. Mandelkow, and D. J. Müller. 2013. The fuzzy coat of pathological human Tau fibrils is a two-layered polyelectrolyte brush. Proceedings of the National Academy of Sciences 110(4):E313.
29. Moreno-Herrero, F., M. Perez, A. M. Baro, and J. Avila. 2004. Characterization by atomic force microscopy of Alzheimer paired helical filaments under physiological conditions. Biophys J 86(1 Pt 1):517-525.
30. Sweers, K. K. M., I. M. J. Segers-Nolten, M. L. Bennink, and V. Subramaniam. 2012. Structural model for [small alpha]-synuclein fibrils derived from high resolution imaging and nanomechanical studies using atomic force microscopy. Soft Matter 8(27):7215-7222.
31. Smith, J. F., T. P. Knowles, C. M. Dobson, C. E. Macphee, and M. E. Welland. 2006. Characterization of the nanoscale properties of individual amyloid fibrils. Proc Natl Acad Sci U S A 103(43):15806-15811.
32. Adamcik, J., A. Berquand, and R. Mezzenga. 2011. Single-step direct measurement of amyloid fibrils stiffness by peak force quantitative nanomechanical atomic force microscopy. Appl Phys Lett 98(19):193701.
33. Adamcik, J., J. M. Jung, J. Flakowski, P. De Los Rios, G. Dietler, and R. Mezzenga. 2010. Understanding amyloid aggregation by statistical analysis of atomic force microscopy images. Nat Nanotechnol 5(6):423-428.
34. Adamcik, J., and R. Mezzenga. 2012. Study of amyloid fibrils via atomic force microscopy. Curr Opin Colloid In 17(6):369-376.
35. Fitzpatrick, A. W., G. M. Vanacore, and A. H. Zewail. 2015. Nanomechanics and intermolecular forces of amyloid revealed by four-dimensional electron microscopy. Proc Natl Acad Sci U S A 112(11):3380-3385.
36. Nassar, R., E. Wong, J. Gsponer, and G. Lamour. 2019. Inverse Correlation between Amyloid Stiffness and Size. Journal of the American Chemical Society 141(1):58-61.
37. Nassar, R., E. Wong, J. M. Bui, C. K. Yip, H. Li, J. Gsponer, and G. Lamour. 2018. Mechanical Anisotropy in GNNQQNY Amyloid Crystals. The Journal of Physical Chemistry Letters 9(17):4901-4909.
38. Engel, M. F. M., L. Khemtémourian, C. C. Kleijer, H. J. D. Meeldijk, J. Jacobs, A. J. Verkleij, B. de Kruijff, J. A. Killian, and J. W. M. Höppener. 2008. Membrane damage by human islet amyloid polypeptide through fibril growth at the membrane. Proceedings of the National Academy of Sciences 105(16):6033-6038.
39. Knowles, T. P., C. A. Waudby, G. L. Devlin, S. I. Cohen, A. Aguzzi, M. Vendruscolo, E. M. Terentjev, M. E. Welland, and C. M. Dobson. 2009. An analytical solution to the kinetics of breakable filament assembly. Science 326(5959):1533-1537.
40. Prusiner, S. B. 2012. Cell biology. A unifying role for prions in neurodegenerative diseases. Science 336(6088):1511-1513.
41. Lamour, G., R. Nassar, P. H. W. Chan, G. Bozkurt, J. Li, J. M. Bui, C. K. Yip, T. Mayor, H. Li, H. Wu, and J. A. Gsponer. 2017. Mapping the Broad Structural and Mechanical Properties of Amyloid Fibrils. Biophysical Journal 112(4):584-594.
42. Pan, K., and Q. Zhong. 2015. Amyloid-like fibrils formed from intrinsically disordered caseins: physicochemical and nanomechanical properties. Soft Matter 11(29):5898-5904.

43. Bortolini, C., N. C. Jones, S. V. Hoffmann, C. Wang, F. Besenbacher, and M. Dong. 2015. Mechanical properties of amyloid-like fibrils defined by secondary structures. Nanoscale 7(17):7745-7752.
44. Wang, W., Z. Guo, J. Sun, and Z. Li. 2017. Nano-mechanical characterization of disassembling amyloid fibrils using the Peak Force QNM method. Biopolymers 107(2):61-69.

FIGURE LEGENDS

Figure 1: (a,b,c) PM-AFM topography images in ambient air of (a) 0N3R, (b) 1N3R, (c) 2N3R, (d) 0N4R, (e) 1N4R, (f) 2N4R Tau fibrils adsorbed onto mica substrate. Below each topography image is represented the corresponding Tau protein structures showing the number of amino□terminal inserts (0N, 1N, and 2N) or carboxyl□terminal microtubule binding domain repeats (3R and 4R). Green arrows indicate fibrils where the protofibrils separation was not seen.

Figure 2: High resolution PM-AFM topography images in ambient air of the studied six tau isoforms 0N3R, 1N3R, 2N3R, 0N4R, 1N4R, and 2N4R fibrils adsorbed onto mica substrate. The images and the line profiles (dashed lines) show clearly the PHF-like aspect of the different Tau isoform fibrillar assemblies.

Figure 3: Electron micrographs of 0N3R, 1N3R, 2N3R, 0N4R, 1N4R, 2N4R Tau fibrils adsorbed onto carbon coated copper grid after negative staining with Uranyl acetate. The boxed regions labeled in each electron micrograph (left panel) were enlarged (right panels) to show that Tau fibrils are flat particles, resembling ribbons, that twist and that are most likely made of two protofilaments. Scale bar, 100nm.

Figure 4: (a,b,c) AM-AFM topography images in air of 0N3R, 1N3R and 2N3R Tau fibrils respectively, adsorbed onto mica substrate. **(d,e,f)** The contour length plots of the different Tau fibrils imaged by AFM, where initial tangents were aligned. **(g,h,i)** Blue open circles corresponds to the deviations $<\delta^2>2D$ to secant midpoints as a function of the distance for Tau fibrils adsorbed on mica. Fits of the worm-like chain model to the data are shown as red lines.

Figure 5: (a,b,c) AM-AFM topography images in air of 0N4R, 1N4R and 2N4R Tau fibrils respectively, adsorbed onto mica substrate. **(d,e,f)** The contour length plots of the different Tau fibrils imaged by AFM, where initial tangents were aligned. **(g,h,i)** Blue open circles corresponds to the deviations $<\delta^2>2D$ to secant midpoints as a function of the distance for Tau fibrils adsorbed on mica (blue open circles). Fits of the worm-like chain model to the data are shown as red lines.

Figure 6: a. Inverse correlation between Young's modulus and the rectangular sectional area of amyloids fibrils as reported by Nassar et al.(36) The dashed line represents the fitting curve described as $Y=\alpha C^{\beta}$ with Y = Young's modulus, C= rectangular cross sectional area, $\alpha=1.31x10^{-}$

[28] and β=2.2). The black squares correspond to the morphological and mechanical properties of experimental measurements for different amyloids (15, 36, 41-44). The blue triangles and red circles represent the predicted and experimental Young's moduli of tau fibrils, respectively. **b**. Bending rigidity values (κ) as a function of the second moment of area (I) of Tau fibrillar isoform considered as tape-like-model. The diagonal colored bands correspond to the range of the axial Young modulus (K) as determined by Knowles et al.(18). The background coloring has been adapted from Knowles et al. (18) for comparison purposes. The gray region is representative of elastic moduli of materials held together by strong intermolecular forces such as covalent bonds in metals. The dark blue region corresponds to hydrogen-bonded protein nanostructures and represents the range of Young moduli of non-prion amyloid fibrils as determined in previous studies (18, 31). The green region represents materials that are held together by amphiphilic interactions which are defined as defined as "intermolecular interactions that are mediated by the variable side chains in the absence of a rigid framework provided by intermolecular hydrogen bonding"(18, 35). The yellow region is the region corresponding to entropic elasticity.

Figure 7: Topography image (first column), Spring constant map (second column) and the Young modulus map of Tau 0N3R, 1N3R and 2N3R fibrils, obtained with QI mode in PBS buffer at a force setpoint of 0.55 nN at an indentation speed of 15 µm/s.

Figure 8: Topography image (first column), Spring constant map (second column) and the Young modulus map of Tau 0N4R, 1N4R and 2N4R fibrils, obtained with QI mode in PBS buffer at a force setpoint of 0.55 nN at an indentation speed of 15 µm/s.

Table 1: Morphological and mechanical properties of the different Tau fibrils type. The persistence lengths were determined by the mean square of the deviations $<\delta^2>_{2D}$ to secant midpoints approach from AFM images of Tau fibrils adsorbed onto mica and performed in air at room temperature. The tape model was used to calculate the second moment of area (I) of fibrils using the lowest energy bending mode.

	Morphological properties		**Nanomechanical properties**			
Tau fibril isoforms	**AFM Height (nm)**	**TEM Width (nm)**	**P*l* (µm) in air**	**I_{min} ($.10^{-34} m^4$)**	**K ($.10^{-27}$ N.m^2)**	**E (MPa)**
0N3R	5.7 ± 0.9 (n=157)	12.3± 0.5 (n=34)	1.2±0.5 (n=140)	1.9	4.9±2.0	26.0
0N4R	5.9 ± 0.9 (n=196)	13.8±2 (n=40)	2.0±0.4 (n=133)	2.4	8.2±1.6	34.8
1N3R	6.6 ± 1.2 (n=90)	12.1±1.1 (n=36)	1.1± 0.2 (n=119)	2.9	4.5±0.8	15.6
1N4R	7.0 ± 1.0 (n=168)	12.3±0.8 (n=35)	2.8±0.5 (n=137)	3.5	11.5±0.2	32.8
2N3R	5.2 ± 1.1 (n=241)	12.4±1.1 (n=32)	1.2±0.2 (n=284)	1.4	4.9±0.8	34.0
2N4R	6.7 ± 1.0 (n=108)	13.4±0.7 (n=31)	1.9±0.4 (n=206)	3.3	7.8±1.6	23.3

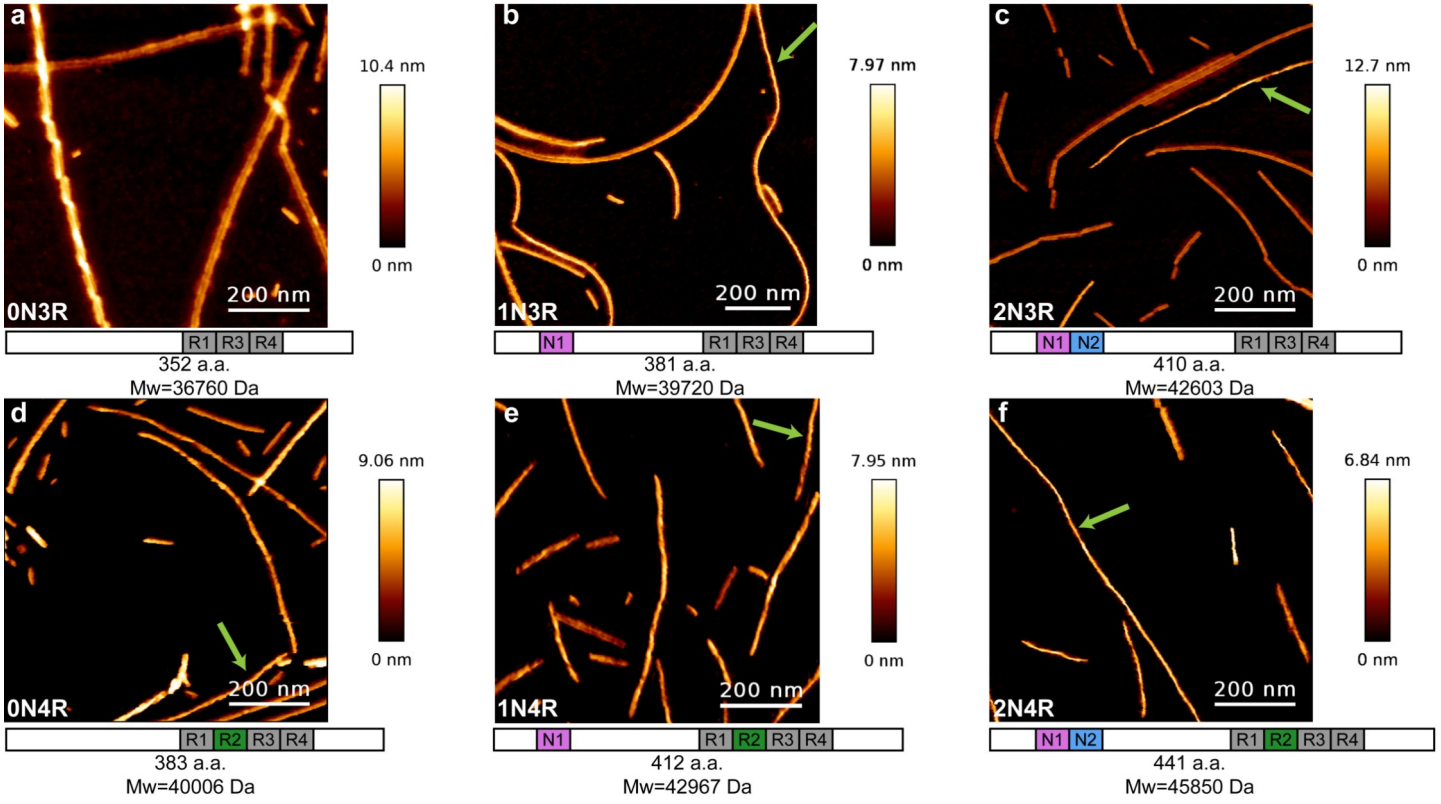
a
10.4 nm
0 nm
200 nm
0N3R
R1 R3 R4
352 a.a.
Mw=36760 Da
b
7.97 nm
0 nm
200 nm
1N3R
N1 R1 R3 R4
381 a.a.
Mw=39720 Da
c
12.7 nm
0 nm
200 nm
2N3R
N1 N2 R1 R3 R4
410 a.a.
Mw=42603 Da
d
9.06 nm
0 nm
200 nm
0N4R
R1 R2 R3 R4
383 a.a.
Mw=40006 Da
e
7.95 nm
0 nm
200 nm
1N4R
N1 R1 R2 R3 R4
412 a.a.
Mw=42967 Da
f
6.84 nm
0 nm
200 nm
2N4R
N1 N2 R1 R2 R3 R4
441 a.a.
Mw=45850 Da

Fibrils 0N3R

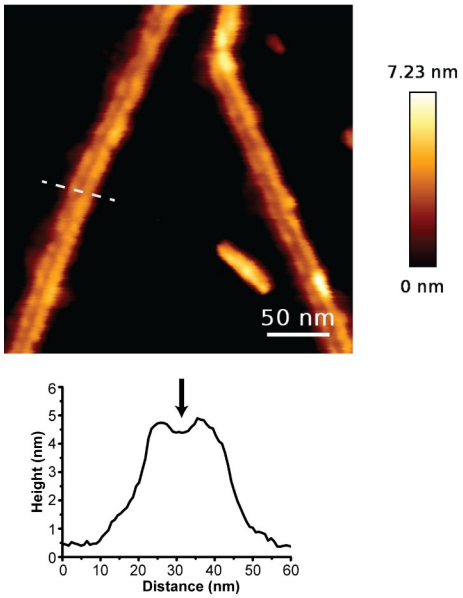

Fibrils 1N3R

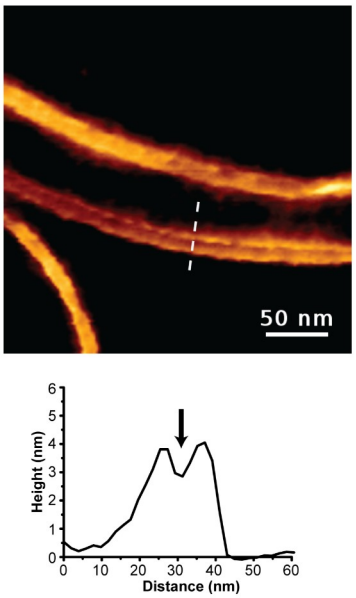

Fibrils 2N3R

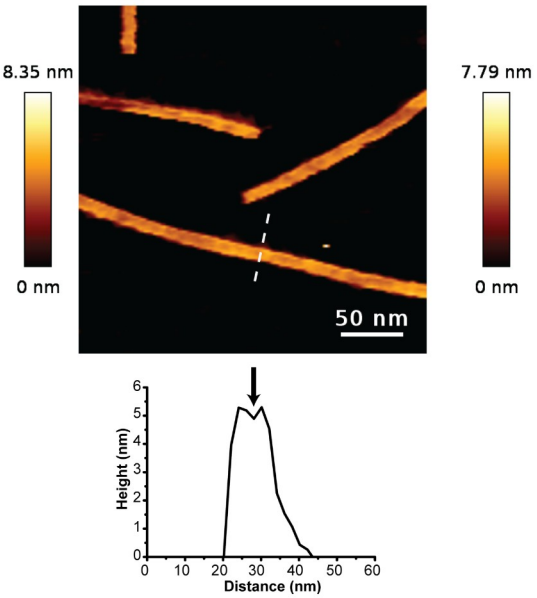

Fibrils 0N4R

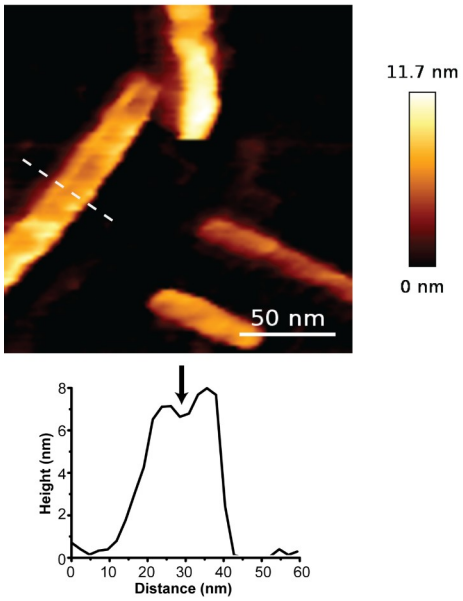

Fibrils 1N4R

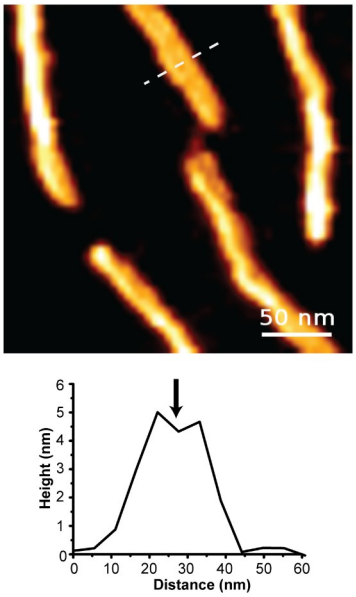

Fibrils 2N4R

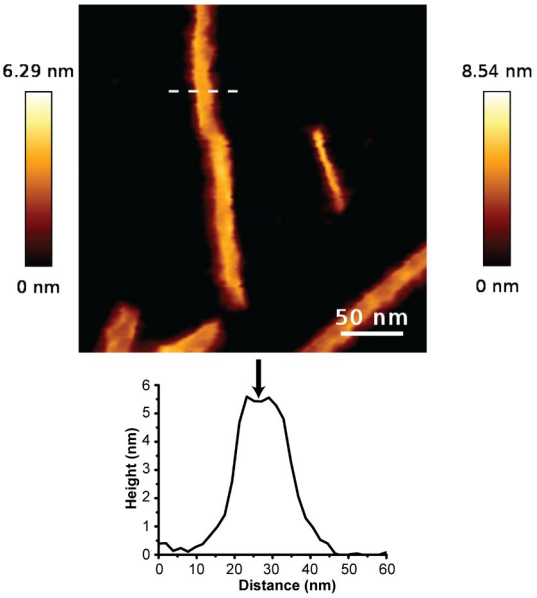

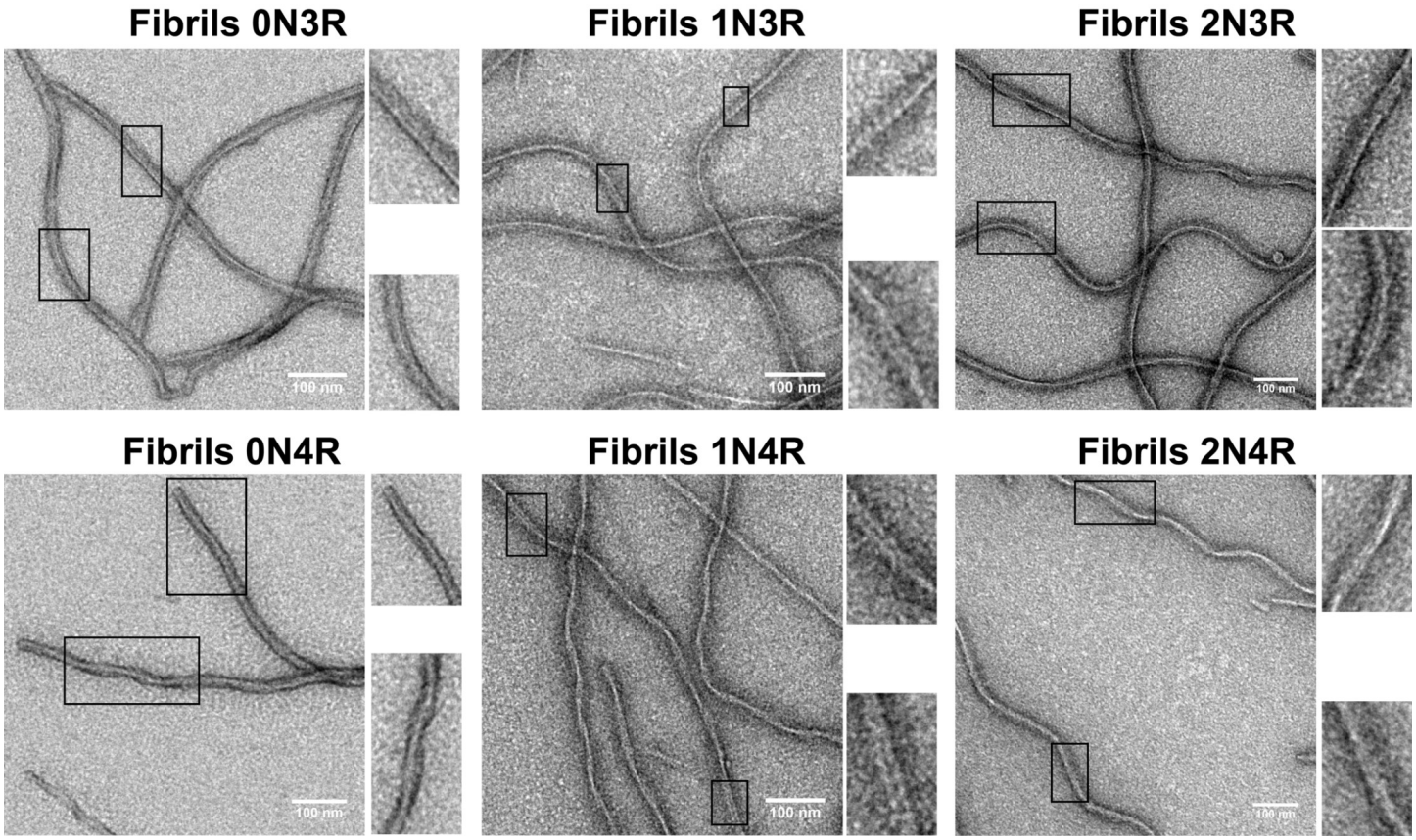
Fibrils 0N3R
Fibrils 1N3R
Fibrils 2N3R
Fibrils 0N4R
Fibrils 1N4R
Fibrils 2N4R
100 nm

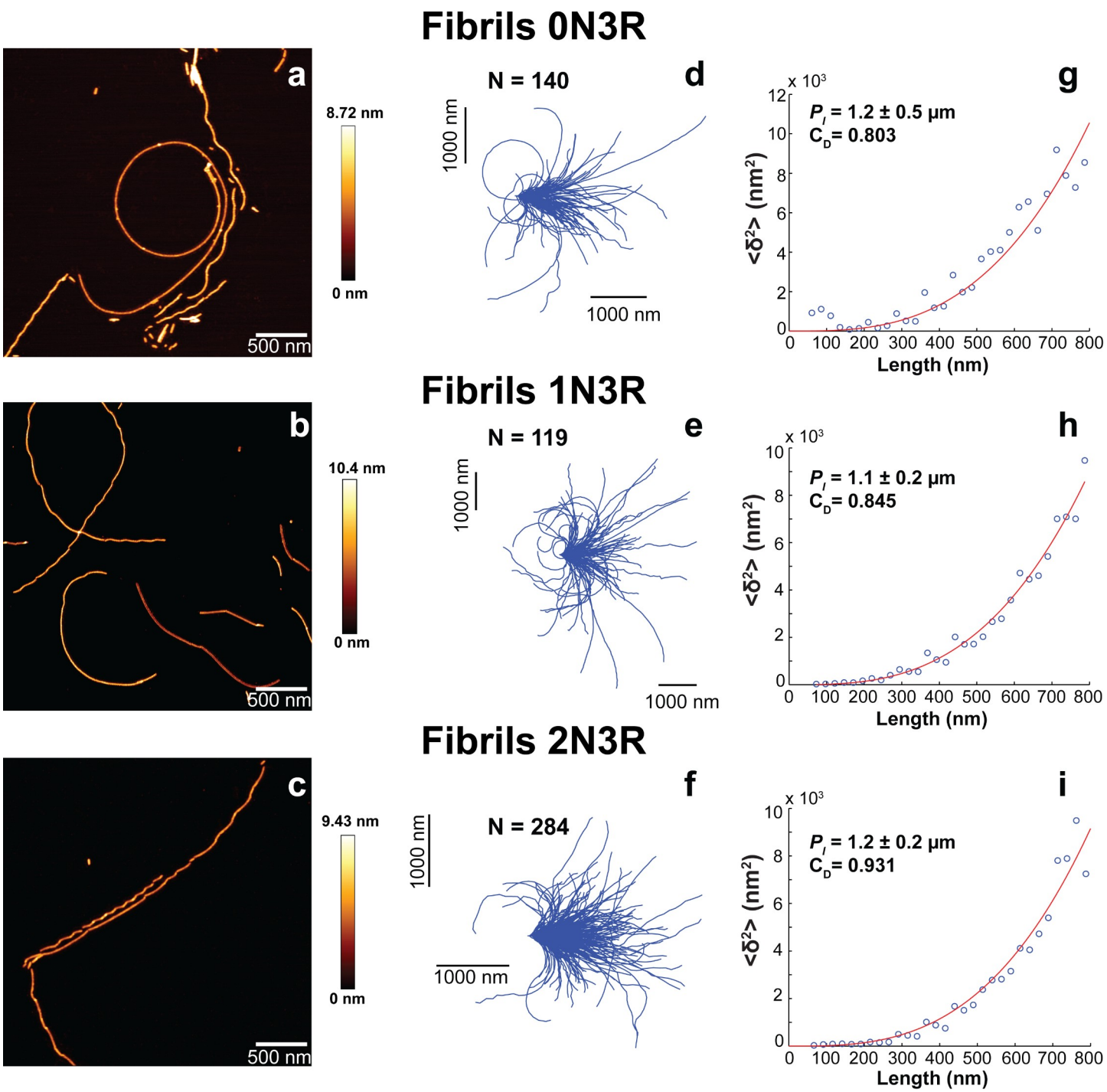
Fibrils 0N3R
a
8.72 nm
0 nm
500 nm
N = 140
d
1000 nm
1000 nm
g
x 10³
P_l = 1.2 ± 0.5 µm
C_D= 0.803
<δ²> (nm²)
Length (nm)
Fibrils 1N3R
b
10.4 nm
0 nm
500 nm
N = 119
e
1000 nm
1000 nm
h
x 10³
P_l = 1.1 ± 0.2 µm
C_D= 0.845
<δ²> (nm²)
Length (nm)
Fibrils 2N3R
c
9.43 nm
0 nm
500 nm
N = 284
f
1000 nm
1000 nm
i
x 10³
P_l = 1.2 ± 0.2 µm
C_D= 0.931
<δ²> (nm²)
Length (nm)

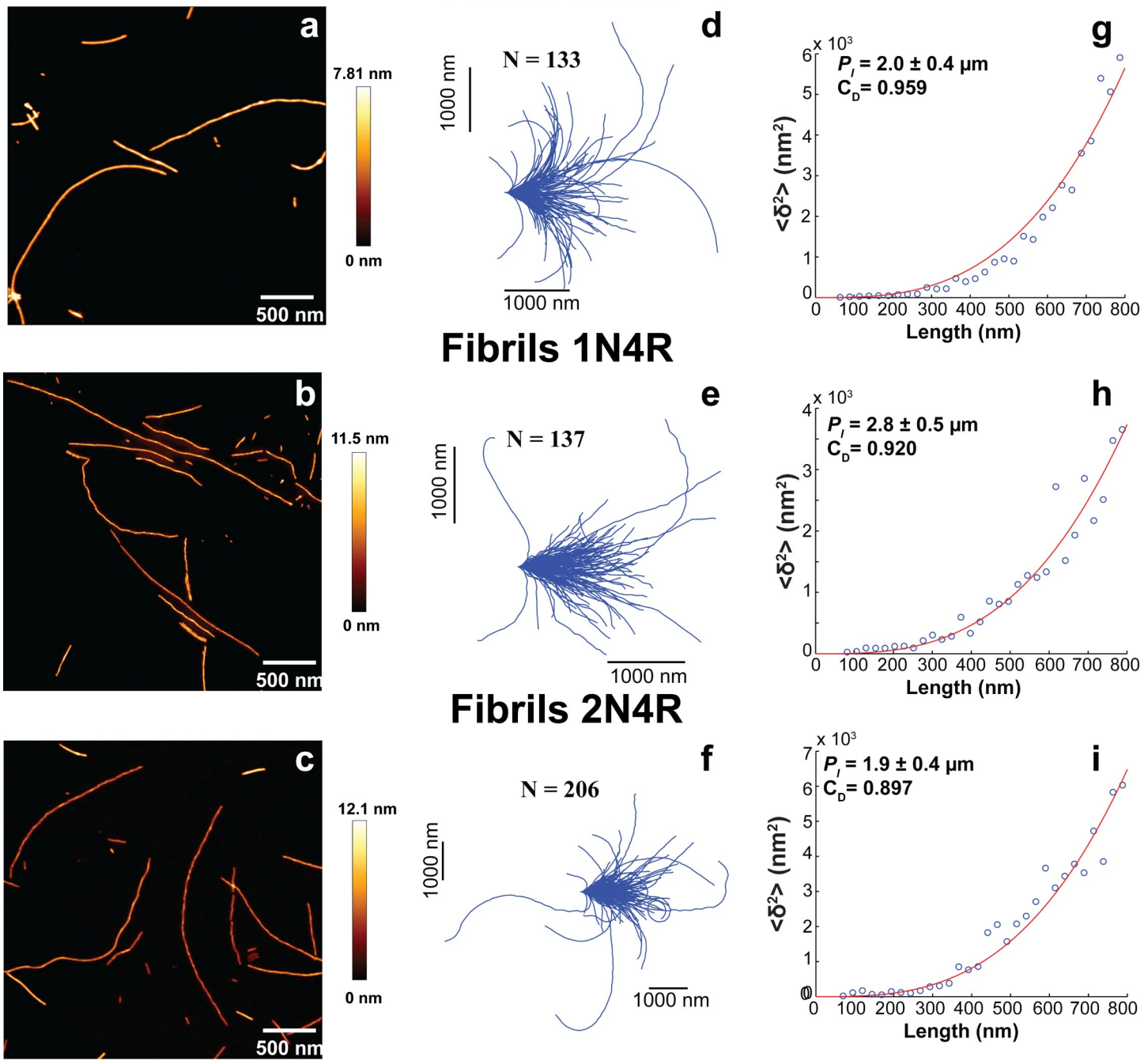
Fibrils 0N4R
Fibrils 1N4R
Fibrils 2N4R
a
b
c
d
e
f
g
h
i
7.81 nm
0 nm
11.5 nm
0 nm
12.1 nm
0 nm
500 nm
500 nm
500 nm
N = 133
N = 137
N = 206
1000 nm
1000 nm
1000 nm
1000 nm
1000 nm
1000 nm
x 10³
P_l = 2.0 ± 0.4 µm
C_D = 0.959
x 10³
P_l = 2.8 ± 0.5 µm
C_D = 0.920
x 10³
P_l = 1.9 ± 0.4 µm
C_D = 0.897
<δ²> (nm²)
Length (nm)
<δ²> (nm²)
Length (nm)
<δ²> (nm²)
Length (nm)

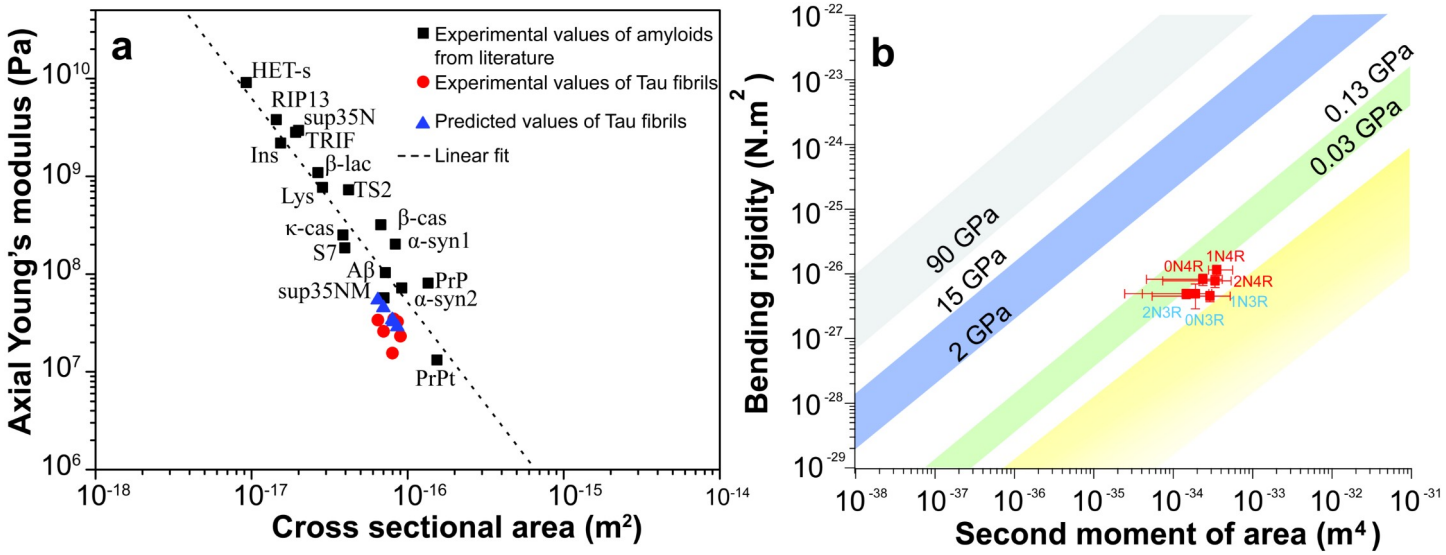
a
Experimental values of amyloids from literature
Experimental values of Tau fibrils
Predicted values of Tau fibrils
Linear fit
HET-s
RIP13
sup35N
TRIF
Ins
β-lac
Lys
TS2
β-cas
κ-cas
α-syn1
S7
Aβ
PrP
sup35NM
α-syn2
PrPt
Axial Young's modulus (Pa)
Cross sectional area (m²)
b
90 GPa
15 GPa
2 GPa
0.13 GPa
0.03 GPa
0N4R
1N4R
2N4R
1N3R
2N3R
0N3R
Bending rigidity (N.m²)
Second moment of area (m⁴)

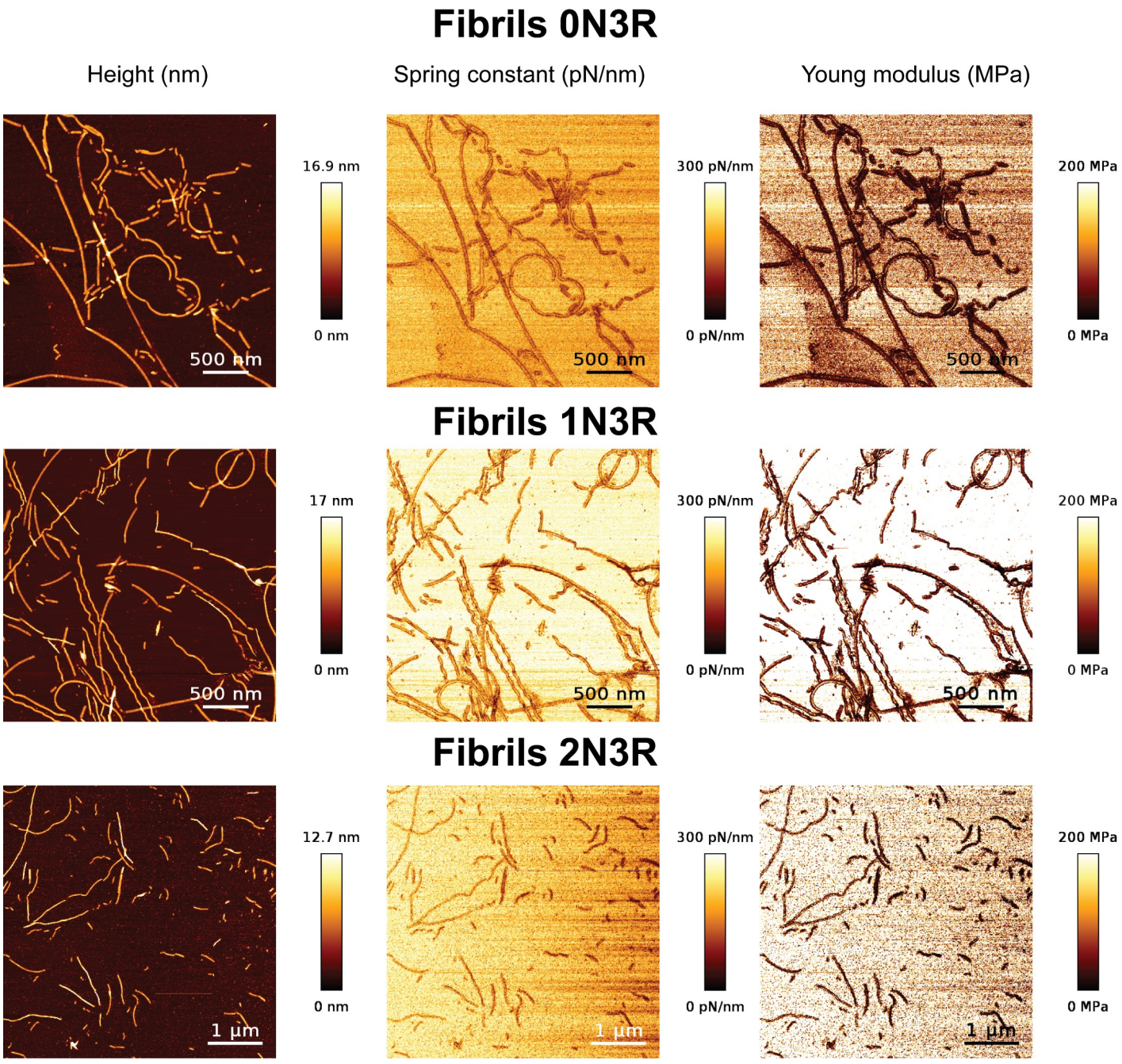
Fibrils 0N3R
Height (nm)
Spring constant (pN/nm)
Young modulus (MPa)
16.9 nm
0 nm
300 pN/nm
0 pN/nm
200 MPa
0 MPa
500 nm
Fibrils 1N3R
17 nm
0 nm
300 pN/nm
0 pN/nm
200 MPa
0 MPa
500 nm
Fibrils 2N3R
12.7 nm
0 nm
300 pN/nm
0 pN/nm
200 MPa
0 MPa
1 µm

Fibrils 0N4R

Height (nm) | Spring constant (pN/nm) | Young modulus (MPa)

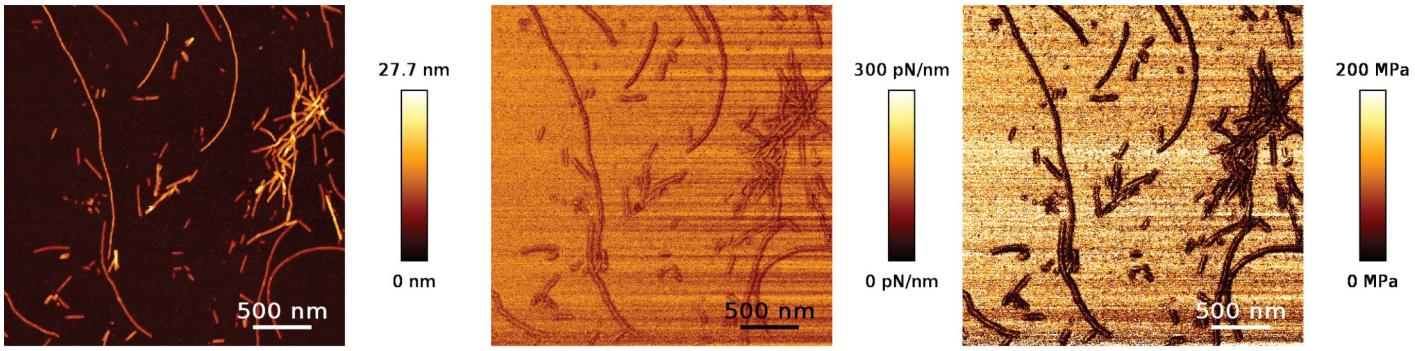

Fibrils 1N4R

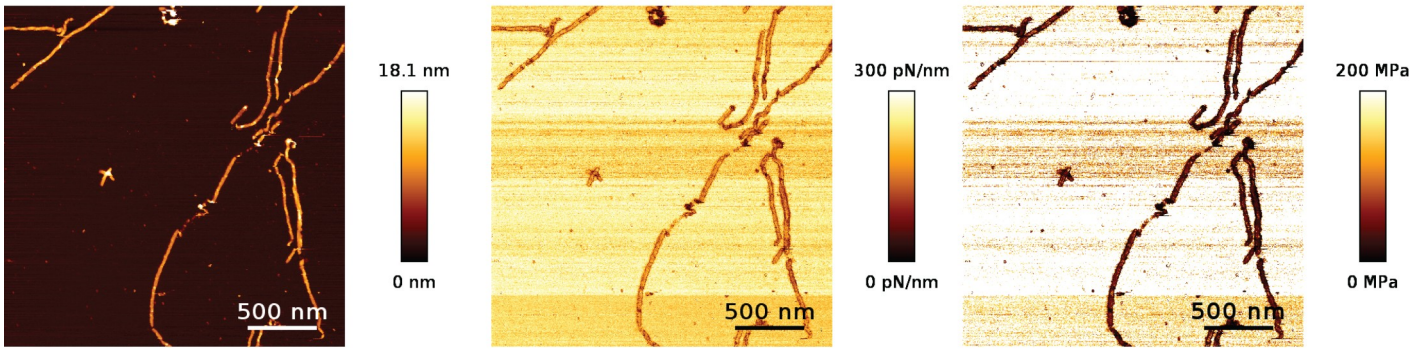

Fibrils 2N4R